Chemical Science

ROYAL SOCIETY OF CHEMISTRY

EDGE ARTICLE

View Article Online
View Journal | View Issue

Cite this: *Chem. Sci.*, 2026, **17**, 2210

All publication charges for this article have been paid for by the Royal Society of Chemistry

Received 26th August 2025
Accepted 13th November 2025

DOI: 10.1039/d5sc06522d

rsc.li/chemical-science

Construction of a built-in electric field in Mo-doped Ni/WO_3 to enhance asymmetric charge distribution for efficient overall water splitting

Yang Sun, Fan Yang, * Kexin Wei, Siyuan Sun, Li Sun, Junpu An, Chunhui Yu, Qing Guo, Conghan Zhang, Guang Ma, Hongchen Liu and Yongfeng Li *

Constructing an asymmetric charge distribution and built-in electric field (BIEF) has proven to be an effective strategy for enhancing the catalytic performance of both hydrogen evolution reaction (HER) and oxygen evolution reaction (OER) catalysts. Herein, a Mo-doped Ni/WO_3 heterojunction catalyst was immobilized on Ni foam for enhancing the performance of the HER and OER. The constructed Ni/WO_3 heterointerface facilitates electron transport, while the incorporation of Mo further amplifies charge asymmetry in the interfacial region. The optimized Mo_3–Ni/WO_3 catalyst exhibits excellent performance, requiring only 13 mV and 328 mV overpotential to reach current densities of 10 and 100 mA cm^{-2} for the HER and OER, respectively. Besides, it maintains stable overall water splitting performance at 100 mA cm^{-2} for 90 h. The asymmetric distribution of Ni/WO_3 interfacial charge is promoted and electron transport is enhanced by Mo doping. Theoretical results show that element doping in the heterostructure turns W sites into additional adsorption centers, optimizing the energetics of H* adsorption during the HER. Mo doping reduces the work function (φ) of Mo_3–Ni/WO_3, promoting efficient electron transfer and lowering the energy barrier for intermediate formation, thereby enhancing OER activity. This strategic modulation of charge asymmetry in heterojunction architectures provides a new approach for the rational design of high-performance bifunctional electrocatalysts.

1 Introduction

The growing adoption of renewable energy sources like solar and wind power as sustainable alternatives to fossil fuels demands the development of advanced energy conversion technologies.[1,2] Water electrolysis is a promising method for producing high-energy-density hydrogen with zero carbon emissions.[3,4] However, its practical use is limited by the slow kinetics of the HER and OER, which require high overpotentials and reduce efficiency.[5,6] Developing bifunctional electrocatalysts capable of driving both reactions has become a key strategy. This simplifies electrolyzer design, lowers costs, and improves reaction balance and compatibility.[7,8] Current design strategies for high-performance, stable bifunctional catalysts include heterojunction electronic structure modulation and doping engineering. However, the integration of the aforementioned regulatory strategies for the HER/OER with different reaction pathways remains to be thoroughly investigated.[9] Consequently, the simultaneous regulation of HER and OER performance through the application of heterojunctions and elemental doping engineering has become a key research focus to enable competitive practical bifunctional catalysts for the HER/OER.[10]

Previous studies have shown that the design of dynamic adaptive heterostructure bifunctional catalysts is an effective strategy for total water hydrolysis. This strategy indicates that the catalyst will undergo dynamic electron regulation to meet the potential requirements of the HER and OER, respectively.[11] Nickel-based materials are emerging as promising bifunctional catalysts for the HER and OER due to their cost-effectiveness, intrinsic catalytic activity, and tunable valence states that can adapt to varying reaction conditions.[12,13] Nevertheless, practical implementation of Ni-based systems remains constrained by challenges including agglomerated active sites and diminished utilization efficiency.[14,15] Current optimization strategies to improve site utilization and avoid agglomeration have been dedicated to compositional engineering *via* 3D porous structure construction,[16] heterostructure design,[17] and the electronic regulation strategy.[18] Among these, developing heterostructure materials with metal oxide substrates and a BIEF offers a highly effective approach. Transition metal oxide carriers provide tunable electronic properties and adjustable band structures, creating unique electronic environments that enhance the adsorption energetics of reaction intermediates during the HER and OER.[19,20] This type of metal oxide support has been proved to improve both the intrinsic activity and stability of the

China University of Petroleum Beijing State Key Laboratory of Heavy Oil Processing, Beijing, China. E-mail: yangfan@cup.edu.cn

materials through structural design and electronic modulation. Tungsten trioxide (WO_3), a prototypical semiconductor, shows great promise in catalysis due to its tunable electronic structure, diverse morphology, and excellent chemical stability.[21] Strategic construction of heterointerfaces between WO_3 and active components has been shown to substantially enhance catalytic performance. For example, Zhou *et al.* reported a PtRu alloy catalyst supported on WO_3 with abundant oxygen vacancies by a microwave-assisted approach.[22] The introduction of WO_3 with abundant oxygen vacancies induced electron enrichment on Pt sites, reasonably optimizing the hydrogen recombination process, which improved the electrochemical activity of the HER. However, the application of WO_3 in overall water splitting is limited by intrinsic drawbacks such as low electrical conductivity and inadequate active site density.[23] To further improve the intrinsic activity of WO_3, morphology regulation and defect engineering strategies have been explored. For example, Li *et al.* prepared a nanotube array-like WO_3/W photoanode through the electrochemical anodic oxidation method.[24] The one-dimensional nanotube-like structure of WO_3 and the strong interaction between WO_3 and the W foil carrier promote efficient electron–hole separation and mass transfer, resulting in high photocurrent density.

Additionally, heteroatom doping is an effective strategy to regulate the electronic structure and surface properties of heterojunction materials.[25] By introducing doping elements, the band structure, work function, and charge distribution of the material can be adjusted to optimize the catalytic performance, which contributes to the material exhibiting dual functional properties in overall water splitting. The molybdenum (Mo) element has strong electropositivity, which can significantly regulate the electron distribution and promote the nucleophilic adsorption of water.[26,27] For example, Ge *et al.* synthesized Mo-doped NiCo LDH and the $FeCo_2S_4$ heterostructure through hydrothermal and electrodeposition reactions.[28] The strong redistribution of the charges around metal active sites by Mo doping induced a weakened adsorption energy barrier for intermediates in the HER and OER. Mo element doping effectively regulates charge redistribution in heterojunction structures, offering a viable strategy to control catalyst adsorption and reaction pathways, enabling the catalyst to perform efficiently in both the HER and OER. Consequently, combining elemental doping with heterostructure engineering enables the rational design of composite catalysts, allowing for precise optimization of electronic configurations and surface properties to enhance HER and OER catalytic efficiency.

In this work, a self-supported Mo-doped Ni/WO_3 heterostructure catalyst (Mo_x–Ni/WO_3) was rationally synthesized. The WO_3 nanoarray carrier with a rough surface leads to well-exposed active sites, resulting in a hydrophilic interface between electrodes and electrolytes. It also functions as an electron acceptor, forming a BIEF in conjunction with Ni. The incorporation of Mo induces an enhanced local electrophilic/nucleophilic region in the heterostructure interface, leading to a decreased work function of the material, which constructs the BIEF and accelerates interfacial charge transfer kinetics between WO_3 and Ni active sites. The optimized catalyst Mo_3–Ni/WO_3 achieves ultralow overpotentials of 13 mV and 108 mV to deliver current densities of 10 mA cm^{-2} for the HER and OER, respectively. Density functional theory (DFT) calculations elucidate that W optimizes the adsorption of intermediate H* in the HER process. Meanwhile, the formation of the oxidation state of Ni sites is optimized by doping Mo with high valence, reasonably regulating the adsorption energetics of oxygenated intermediates to boost OER performance. These synergistic effects endow the Mo_3–Ni/WO_3 heterostructure catalyst with superior electrochemical activity, demonstrating its promising potential for alkaline water electrolysis applications.

2 Experimental

2.1 Materials

Nickel foam (NF, thickness is 1.5 mm) was procured from Suzhou Taili Metallic Foam Co., Ltd. Ammonium tungstate ($(NH_4)_{10}H_2(W_2O_7)_6$, 98.5%), potassium hydroxide (KOH, 85%), nickel chloride hexahydrate ($NiCl_2 \cdot 6H_2O$, 99%), sodium molybdate (Na_2MoO_4, 98.5%), sodium citrate dihydrate ($Na_2C_6H_6O_7 \cdot 2H_2O$, 99%), and ruthenium dioxide (RuO_2) were purchased from Aladdin. The commercial Pt/C catalyst (20 wt%) and lauryl sodium sulfate (SDS, 99%) were gained from Innochem. Absolute ethyl alcohol (AR, 99%) and ammonia were purchased from Tianjin Jindong Tianzheng Fine Chemical Reagent Factory.

2.2 Synthesis of WO_3/NF

A Ni foam substrate (3 × 4 cm) was thoroughly washed with acetone, HCl (1 M), and deionized water to clean the surface for further use. Then, 60 mM of $(NH_4)_{10}H_2(W_2O_7)_6$, and 100 mM of sodium SDS were dissolved in 35 mL of deionized water at 25 °C to form a mixed solution under continuous magnetic stirring for 3 h. After that, the treated Ni foam was added to the mixed solution and stirring was continued for 1 h. The resultant mixture was subsequently introduced into a Teflon-lined stainless-steel autoclave and subjected to hydrothermal treatment at 200 °C for 6 hours under autogenous pressure in a precisely temperature-controlled reaction chamber. Finally, the products were washed with deionized water and ethanol after natural cooling, and dried under vacuum at 50 °C. WO_3/NF was prepared by a subsequent calcination under an Ar atmosphere at 400 °C for 2 h.

2.3 Synthesis of Mo_x–Ni/WO_3

A homogeneous solution was prepared by dispersing 4 mmol of $NiCl_2 \cdot 6H_2O$, 4.3 mmol of $Na_2C_6H_6O_7 \cdot 2H_2O$, and 3 mmol of Na_2MoO_4 in 50 mL of deionized water, followed by ultrasonication for 10 minutes. The pH of the resulting solution was adjusted to 10 using ammonia. WO_3/NF (1 × 1 cm^2), a platinum sheet and a Ag/AgCl electrode were used as the working electrode, counter electrode, and reference electrode, respectively. Electrodeposition was performed *via* chronopotentiometry at a constant current density of −0.18 A cm^{-2} for 600 s. The product was named Mo_3–Ni/WO_3. Ni^{2+} and Mo^{6+} were reduced on the prepared WO_3 substrate with a rough surface through

induced co-deposition. $Na_2C_6H_6O_7 \cdot 2H_2O$ serves as a complexing agent by forming a stable complex with Ni^{2+}, thereby shifting the reduction potential to more negative values. The catalyst loading mass of Mo_3–Ni/WO_3 is shown in Table S1. To investigate the influence of precursor concentration and deposition time, a series of Mo_x–Ni/WO_3 electrodes were synthesized. Specifically, electrodes with Na_2MoO_4 concentrations of 1, 2, and 4 mmol were prepared and labelled as Mo_1–Ni/WO_3, Mo_2–Ni/WO_3, and Mo_4–Ni/WO_3, respectively. Additionally, electrodes with electrodeposition times of 300 s and 900 s were fabricated and denoted as Mo_3–Ni/WO_3-300 and Mo_3–Ni/WO_3-900, respectively.

For comparison, Ni/WO_3 was synthesized without the addition of Na_2MoO_4 in the electrolyte. Mo_3–Ni/NF was synthesized in the same electrolyte with Mo_3–Ni/WO_3 except the treated Ni foam was used as the working electrode.

2.4 Characterization of catalysts

The microstructural features and dimensional parameters of the samples were characterized through advanced electron microscopy techniques, including field-emission scanning electron microscopy (FE-SEM, Hitachi SU8010) and high-resolution transmission electron microscopy (HR-TEM, Tecnai G2 F20). Structural properties and carbon ordering were examined using X-ray diffraction (XRD, Bruker D8 Advance) with Cu Kα radiation ($\lambda = 1.5418$ Å) in conjunction with Raman spectroscopic analysis (Horiba Jobin Yvon T6400) employing a 532 nm excitation laser. And metal content was determined by inductively coupled plasma optical emission spectrometry (ICP OES, Optima 7300 V). Surface chemical analysis was performed *via* X-ray photoelectron spectroscopy (XPS, Thermo Scientific K-Alpha) utilizing an Al Kα X-ray source with charge neutralization capability. Electron paramagnetic resonance (EPR) spectroscopy (Bruker EMXplus) was utilized to detect the unpaired electron signals of the catalysts. Work function determination was derived from ultraviolet photoelectron spectroscopy (UPS, Thermo SCIENTIFIC Nexsa) with He resonance lines (21.22 eV). The electrochemical behavior was evaluated using a CHI 1130E electrochemical workstation (Shanghai Chenhua Instrument Co., Ltd) configured with a conventional three-electrode arrangement.

2.5 Electrochemical measurements

Electrochemical measurements were performed using a conventional three-electrode configuration, comprising a Hg/HgO reference electrode, Pt sheet counter electrode, and Mo_3–Ni/WO_3 working electrode. The electrocatalytic performance for the HER and OER was evaluated in 1 M KOH electrolyte. Linear sweep voltammetry (LSV) measurements were conducted at a scan rate of 10 mV s^{-1} with 85% *iR* compensation, and all potentials were converted to the reversible hydrogen electrode (RHE) scale using the following conversion: $E_{(RHE)} = E_{(Hg/HgO)} + 0.098 + 0.059 \times pH$, where the electrolyte pH was maintained at approximately 14. Electrochemical impedance spectroscopy (EIS) was employed to determine charge-transfer resistance across a frequency range of 0.01 to 10^5 Hz. The electrochemical surface area (ECSA) was estimated through double-layer capacitance (C_{dl}) measurements derived from cyclic voltammetry (CV) scans in the non-faradaic region at varying scan rates (30–180 mV s^{-1}). Additional CV analyses were performed at 10 mV s^{-1} within a potential window of 0.02–50 mV s^{-1} to investigate hydrogen underpotential deposition. Long-term stability was assessed through LSV comparisons before and after 2000 CV cycles, complemented by chronoamperometric (CA) measurements to evaluate catalytic durability.

Overall water splitting tests were conducted in a homemade two-electrode system with Mo_3–Ni/WO_3 as both the cathode and anode. The LSV curves were obtained in 1 M KOH at a scan rate of 5 mV s^{-1} within 1.1–2.1 V (*vs.* RHE).

The catalyst inks for Pt/C and RuO_2 electrodes were prepared by dispersing 5 mg of each catalyst in a mixed solvent system containing 500 μL of deionized water and ethanol, followed by the addition of 35 μL Nafion solution as a binder. The mixture was subjected to thorough ultrasonication to achieve homogeneous dispersion. Subsequently, 60 μL of the resulting ink was uniformly deposited onto hydrophilic carbon cloth substrates using a precise pipetting technique. The coated electrodes were then air-dried at ambient temperature (28 °C) to ensure proper adhesion and film formation.

3 Results and discussion

3.1 Morphological and structural characterization

The synthetic procedures for hierarchical Mo_x–Ni/WO_3 are illustrated in Fig. 1a. $(NH_4)_{10}H_2(W_2O_7)_6$, and Ni foam were employed as a tungsten source and reducing agent, respectively. SDS was introduced into water to form an immiscible two-phase system, leading to the formation of an oil–water interface.[29] During the hydrothermal process, the precursor nanosheets are assembled at the oil-water interface driven by high temperature and high pressure. With increasing reaction time, additional precursor nanosheets accumulate and stack, leading to the formation of a precursor structure with a rough surface. The vertically oriented-WO_3 with oxygen vacancies was formed by a hydrothermal reaction and calcination process, respectively, which was denoted as WO_3/NF (Fig. S1a). The WO_3/NF architecture, featuring vertically oriented nanosheets and a rough surface, offers an increased ECSA and provides favourable nucleation sites for subsequent metal deposition.[30] The metal sites were reduced on the WO_3 substrate through electrodeposition. SEM and TEM of Mo_3–Ni/WO_3 show the typical morphology of small speres in Fig. 1b and c. To highlight the crucial role of the WO_3 substrate, metal sites are directly electrodeposited on bare NF (Fig. S1b), showing large metal particle morphology compared to Mo_3–Ni/WO_3. The high-resolution transmission electron microscopy (HRTEM) image in Fig. 1d exhibits a well-defined heterogeneous interface in Ni and WO_3. The lattice fringes with spacings of 0.316 and 0.328 nm correspond to the (200) and (102) plane of WO_3, respectively. Furthermore, lattice fringes with a spacing of 0.176 nm are in alignment with the (200) plane of Ni. The HRTEM image failed to show any crystal lattice data related to Mo, suggesting the incorporation of Mo through doping in the Mo_3–Ni/WO_3

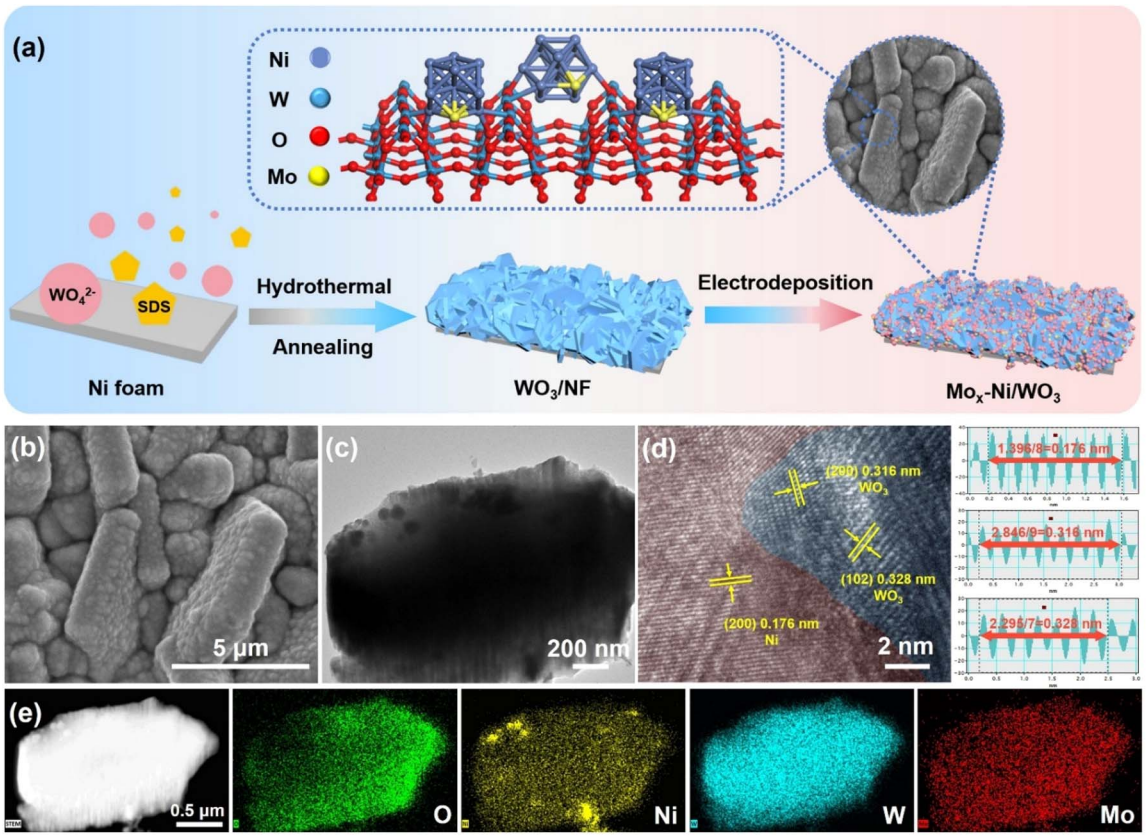

Fig. 1 Schematic illustration for Mo_x–Ni/WO_3 preparation (a), SEM (b), TEM (c), lattice fringe (d), and elemental mapping images (e) of Mo_3–Ni/WO_3.

material. The EDS elemental mapping images in Fig. 1e show that W, Ni, Mo, and O elements are evenly distributed in the catalyst. The elemental contents of Mo_3–Ni/WO_3 tested by EDS are shown in Table S2. The Ni, W, and Mo element contents in Mo_3–Ni/WO_3 were also determined by ICP analysis and were found to be 6.18%, 58.02%, and 1.40%, respectively. The SEM of Ni/WO_3 in Fig. S1c shows a similar morphology to Mo_3–Ni/WO_3, indicating that the formation of the Mo element does not significantly alter the overall structural framework of the material.

XRD analysis was conducted to systematically investigate the crystalline phase structure and composition of Mo_3–Ni/WO_3. Fig. 2a shows the XRD patterns of Mo_3–Ni/NF, WO_3/NF, Ni/WO_3, and Mo_3–Ni/WO_3. Notable diffraction peaks located near 2θ values of 14.32°, 23.92°, 28.35°, 37.22°, 49.83°, 55.55°, and 63.42° align with WO_3 (PDF#08-0634).[23,29] Additionally, the presence of metallic Ni is confirmed by diffraction peaks at 44.75°, 52.23°, and 76.67°, which correspond to Ni (PDF#70-0989). A detailed analysis reveals a notable positive shift in the Ni peak at about 44.75° in the Mo_3–Ni/WO_3 catalyst compared to Ni/WO_3, indicating that Mo enters in the form of element doping.[31] This observation further supports the hypothesis that Mo is predominantly incorporated as a dopant rather than forming discrete phases. Besides, the XRD pattern of Mo_3–Ni/NF only shows the characteristic peaks of Ni.

The chemical bonding states of the surface composition in the prepared catalysts were investigated by XPS.[32] The survey XPS spectrum verified the presence of W, Ni, Mo, and O elements in the Mo_3–Ni/WO_3 catalyst (Fig. S2). The element content tested by XPS is shown in Table S3, which is similar to the EDS result. In the high-resolution Ni 2p XPS spectrum of Mo_3–Ni/WO_3 (Fig. 2b), the peaks at 856.3 eV and 873.9 eV correspond to Ni $2p_{3/2}$ and Ni $2p_{1/2}$ of Ni^{2+}, respectively, with satellite peaks observed at about 862.5 eV and 880.8 eV.[33] Peaks at approximately 852.6 eV and 869.7 eV indicate metallic Ni^0. Notably, Ni $2p_{3/2}$ in Mo_3–Ni/WO_3 (856.4 and 852.8 eV) shows a more significant positive shift compared to that in Ni/WO_3 (856.1 and 852.6 eV), indicating electron loss in Mo_3–Ni/WO_3 due to the incorporation of Mo. The high-resolution W 4f spectrum in Fig. 2c shows two main peaks at approximately 35.5 eV and 37.6 eV, corresponding to $4f_{7/2}$ and $4f_{5/2}$,[5,34] indicating that W in Mo_3–Ni/WO_3 is present as W^{6+}. It is observed that the W incorporation causes a negative shift in Mo_3–Ni/WO_3 when compared with those of Ni/WO_3 (35.6 eV, 37.7 eV) and WO_3/NF (35.7 eV, 37.9 eV), suggesting the formation of a strong electron interaction between Ni and WO_3 upon Mo doping. The Mo 3d high-resolution XPS spectrum of Mo_3–Ni/WO_3 in Fig. 2d shows that the two peaks at about 232.4 and 235.4 eV can be attributed to Mo^{6+}, and a pair of peaks at about 230.8 and 233.9 eV are assigned to Mo^{5+}.[35] These findings indicate that the formation of the heterojunction interface results in an

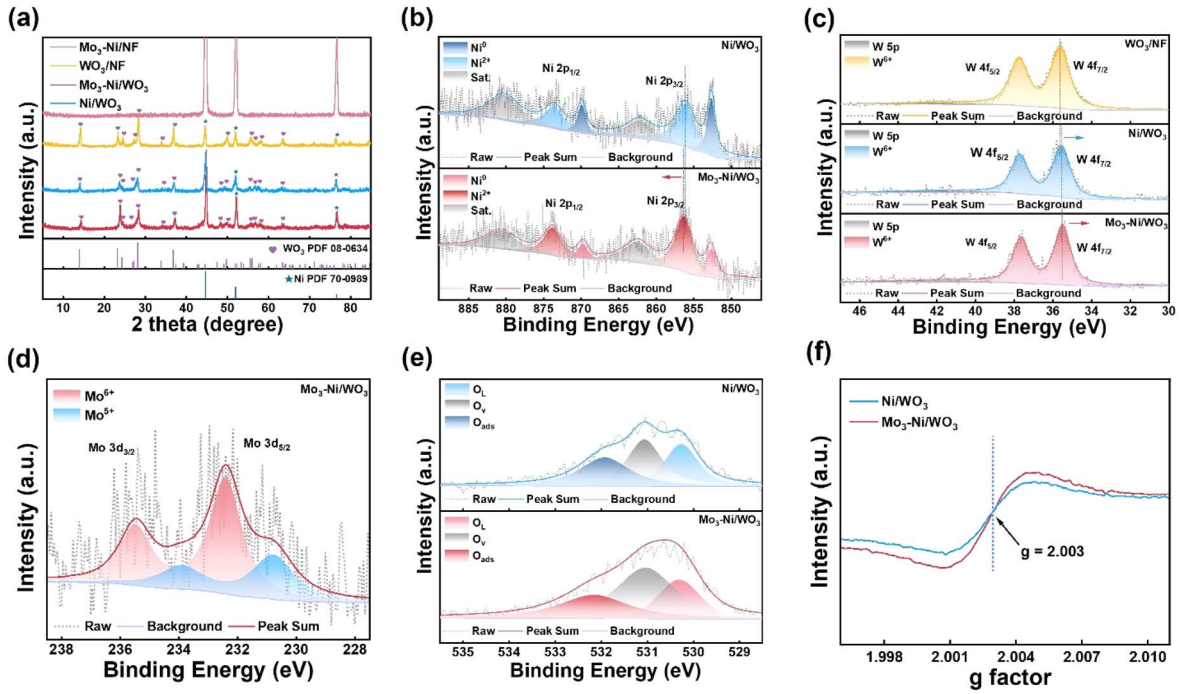

Fig. 2 The XRD patterns of Mo_3–Ni/NF, Ni/WO_3, WO_3/NF, and Mo_3–Ni/WO_3 (a), XPS survey spectra of Ni (b), W (c), Mo (d), and O (e), and EPR signals (f) of Ni/WO_3 and Mo_3–Ni/WO_3.

asymmetric charge distribution between Ni and W. Mo doping further enhances the charge asymmetry, giving rise to a stronger BIEF in Mo_3–Ni/WO_3, which may contribute to improved electrochemical performance. The O 1s XPS spectra of Mo_3–Ni/WO_3 and Ni/WO_3 can be resolved into three characteristic peaks at about 530.3, 531.0, and 532.2 eV ascribed to lattice oxygen (O_L), surface oxygen vacancies (O_V), and chemisorbed or dissociated oxygen species (O_{ads}) as shown in Fig. 2e. The relative O_V percentage of Mo_3–Ni/WO_3 increases compared to that of Ni/WO_3, indicating that Mo doping effectively promotes the formation of surface oxygen defects.[36] To further confirm the presence of oxygen vacancies, the EPR spectrum in Fig. 2f was employed. Both catalysts exhibit a characteristic EPR signal at $g = 2.003$, which is ascribed to unpaired electrons trapped in oxygen vacancy defects.[37] Notably, the significantly enhanced signal intensity observed for Mo_3–Ni/WO_3 provides direct evidence of its higher concentration of oxygen vacancies compared to the undoped counterpart. The ionic radius of Mo differs from those of W and Ni. As a result, Mo doping induces local lattice distortion and triggers a charge compensation effect. To maintain electrical neutrality, the lattice spontaneously generates positively charged oxygen vacancy defects as compensatory species.[37] The oxygen vacancies play a crucial role in enhancing interfacial charge transfer, which is beneficial to reduce the energy barrier for the O* → OOH* transformation during the OER process.[38] Furthermore, contact angle measurements reveal distinct interfacial wettability, while the bare Ni foam substrate maintains a finite contact angle (Fig. S3); the optimized Mo_3–Ni/WO_3 catalyst demonstrates hydrophilic behaviour with instantaneous spreading and complete infiltration of water droplets. The excellent hydrophilicity of Mo_3–Ni/WO_3 could be partially attributed to its distinct nanoarray structure. This structure is advantageous for facilitating the contact between the electrode and the electrolyte, as well as the detachment of bubbles during the electrochemical process.[39,40]

3.2 Electrochemical measurements for the HER

The HER activities of catalysts were evaluated in 1.0 M KOH using a standard three-electrode system. Fig. 3a and b present the *iR*-corrected LSV curves for different catalysts and the corresponding overpotentials at different current densities. It is revealed that Mo_3–Ni/WO_3 achieves 10 mA cm^{-2} at an overpotential of 13 mV, exhibiting a significant improvement compared to Ni/WO_3 (18 mV), which indicates that Mo doping of the Ni/WO_3 heterojunction interface can promote HER performance. Mo_3–Ni/WO_3 also exhibits superior catalytic performance to commercial Pt/C (30 mV@10 mA cm^{-2}), being much lower than that of WO_3/NF (36 mV), Mo_3–Ni/NF (55 mV), and NF (122 mV). The kinetic changes of prepared catalysts can be proved by Tafel plots in Fig. 3c. The Tafel slope of Mo_3–Ni/WO_3 is as low as 37 mV dec^{-1}, which is close to that of Pt/C (25 mV dec^{-1}) and lower than those of Ni/WO_3 (47 mV dec^{-1}), WO_3/NF (62 mV dec^{-1}), Mo_3–Ni/NF (72 mV dec^{-1}), and NF (111 mV dec^{-1}). The decreased Tafel slope of Mo_3–Ni/WO_3 indicates that the rate-determining step (RDS) has shifted desorption.[41] Compared to the reference materials depicted in Fig. 3d, Mo_3–Ni/WO_3 exhibits the superior electrochemical performance. Meanwhile, the EIS results reveal that Mo_3–Ni/WO_3 exhibits the lowest charge transfer resistance (R_{ct}), which

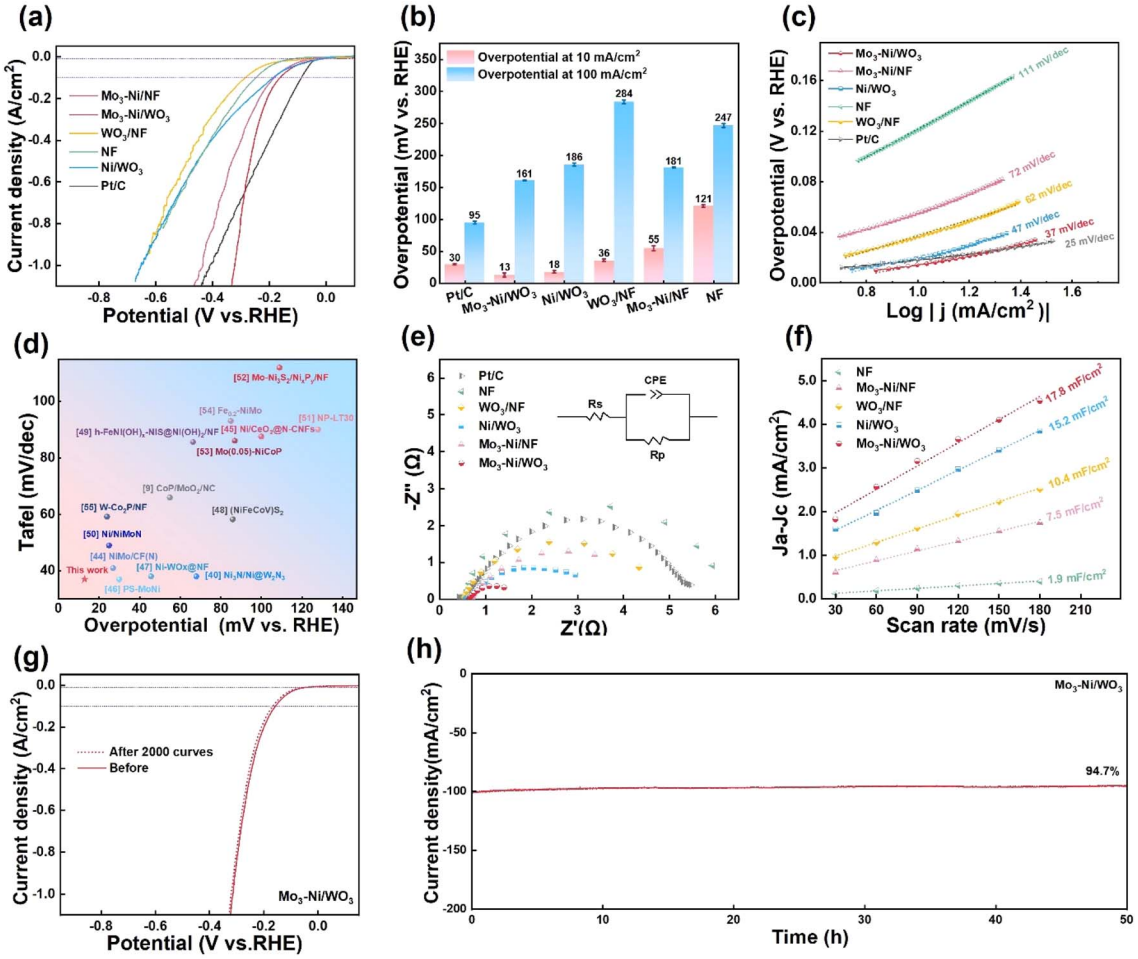

Fig. 3 Polarization LSV curves toward the HER in 1.0 M KOH (a), the overpotentials of obtained samples at different current densities (overpotential values were obtained from the average of 3 measurements) (b), Tafel slopes (c) of Mo_3–Ni/NF, Ni/WO_3, WO_3/NF, Mo_3–Ni/WO_3, NF, and commercial Pt/C, comparison of the HER performance of Mo_3–Ni/WO_3 with other recently reported electrocatalysts[44–55] (d), the Nyquist plot (e) and C_{dl} values (f) of Mo_3–Ni/NF, Ni/WO_3, WO_3/NF, Mo_3–Ni/WO_3, NF, and commercial Pt/C, the LSV polarization curves of Mo_3–Ni/WO_3 before and after 2000 CV cycles (g), and the chronopotentiometry test of Mo_3–Ni/WO_3 at an initial current of 100 mA cm^{-2} for 50 h (h).

further substantiates that Mo doping at the Ni/WO_3 heterojunction interface significantly improved the charge transfer efficiency. Notably, compared to Mo_3–Ni/NF, the excellent performance of the material is also partially attributed to the nanoarray morphology of the WO_3 substrate. The WO_3 substrate functions as an electron acceptor, forming a BIEF in conjunction with Ni. Besides, the ECSA, based on double-layer capacitance (C_{dl}), can be determined through CV tests conducted on prepared catalysts at different scan rates as shown in Fig. S4.[42] As shown in Fig. 3e, Mo_3–Ni/WO_3 possessed the largest double-layer capacitance (17.8 mF cm^{-2}), higher than that of Ni/WO_3 (15.2 mF cm^{-2}), WO_3/NF (10.4 mF cm^{-2}), Mo_3–Ni/NF (7.5 mF cm^{-2}), and NF (1.9 mF cm^{-2}), which implies that the Mo_3–Ni/WO_3 catalyst possesses the highest intrinsic HER activity. This result indicates that Mo-doping of the heterogeneous interfaces provides large ECSA for the electrocatalytic process. Furthermore, the LSV polarization curves of Mo_3–Ni/WO_3 remained almost unchanged significantly after 2000 CV cycles compared to the initial one in Fig. 3g. The chronoamperometric response of Mo_3–Ni/WO_3 was recorded at a current density of 10 and 100 mA cm^{-2} for 50 h as shown in Fig. S5 and 3h, demonstrating the excellent electrochemical durability. Fig. S6a–c display the Bode phase angle plots of Mo_3–Ni/WO_3, Ni/WO_3, and WO_3/NF measured at various applied potentials, while Fig. S6d illustrates the dynamic variation of the phase angle as a function of the applied potential. A smaller phase angle in the low-frequency region corresponds to faster HER kinetics and a higher electron transfer rate for the optimal sample. Compared with Ni/WO_3, and WO_3/NF, the phase angle of Mo_3–Ni/WO_3 exhibits a significant change with increasing applied voltage, indicating enhanced HER kinetics. These results suggest that both W and Ni can serve as active sites for the HER. The excellent HER performance of Mo_3–Ni/WO_3 can be attributed to the unique Mo-doped Ni/WO_3 heterojunction interface, which indicates that the enhanced charge transport kinetics at the heterojunction interface improves the H* adsorption/desorption efficiency during the HER. The large size of the nanoarray topography offers a large electrochemical

surface area and enhanced hydrophilicity, thereby facilitating a more efficient mass transfer process during electrochemical reactions.[43]

To demonstrate the improvement in hydrogen desorption on Mo doping, CV scanning among Mo_3–Ni/WO_3 and Ni/WO_3 was conducted at different scan rates. As shown in Fig. 4a–c, both Mo_3–Ni/WO_3 and Ni/WO_3 catalysts exhibit pseudocapacitive behaviour as the scan rate increases, which indicates the occurrence of a reversible redox process involving intermediates.[56] The enhanced hydrogen desorption peak intensities of Mo_3–Ni/WO_3 illustrates the increased amount of desorbed hydrogen.[57] Besides, the displacement of the hydrogen desorption peak is demonstrated by CV scanning in Fig. 4d. Compared with Ni/WO_3, Mo_3–Ni/WO_3 exhibits a notably reduced slope, indicating the enhanced hydrogen desorption kinetics.[22,58]

This result demonstrates that the enhanced charge asymmetry induced by Mo doping results in improved electron transport efficiency in the heterojunction interface, which enhances the efficiency of intermediate product adsorption/desorption during the HER process.

To further investigate the energy band structure and electronic states of prepared catalysts, the UPS spectra were obtained as shown in Fig. 4e. The moderate valence band maximum (E_v) value of Mo_3–Ni/WO_3 (2.63 eV) is lower than that of Ni/WO_3 (2.68 eV) and WO_3/NF (2.72 eV), indicating lower density of states around the Fermi level (E_f), which suggests improved adsorption for intermediates.[59] The work function of prepared catalysts was calculated from secondary electron cut-off energy. As illustrated in Fig. 4e, the work function of Mo_3–Ni/WO_3 (3.82 eV) is lower than that of Ni/WO_3 (4.14 eV) and WO_3/NF (4.41 eV). The energy band contact diagrams of Mo_3–Ni/WO_3, Ni/WO_3, and WO_3/NF are presented in Fig. 4f. The formation of Ni/WO_3 heterostructures facilitates the transfer of electrons from Ni to WO_3, while the incorporation of the Mo element in the Mo_3–Ni/WO_3 catalyst results in stronger electron interaction and an enhanced BIEF, which exhibits a more efficient electron transfer process.

Furthermore, the effects of different Mo doping amounts and different electrodeposition times on electrochemical performance are discussed in Fig. S7. The SEM image of Mo_x–Ni/WO_3 under different Mo contents is shown in Fig. S8, which exhibits similar morphology. Combined with XRD and XPS characterization, Mo in the form of doping in the material does not affect the intrinsic morphology. This result indicates that Mo doping has a critical threshold for the positively modulating the electronic structure of the Ni/WO_3 heterojunction. The loading capacity of the Ni active site is determined by different electrodeposition times; the SEM image is shown in Fig. S9. When the electrodeposition time is 300 s, the less active sites on Mo_3–Ni/WO_3-300 exhibit poor HER performance. The Mo_3–Ni/WO_3-900 catalyst shows agglomerated active sites, exhibiting a covered Ni/WO_3 heterojunction interface, which results in poor electron transport. In addition, SEM and XRD of Mo_3–Ni/WO_3 after HER stability tests indicate that the original morphology and structure can be well maintained (Fig. S10a and b). XPS of Mo_3–Ni/WO_3 after HER stability testing also showed almost no changes in the valence states of the elements in Fig. S10c–f, proving the excellent HER stability for Mo_3–Ni/WO_3.

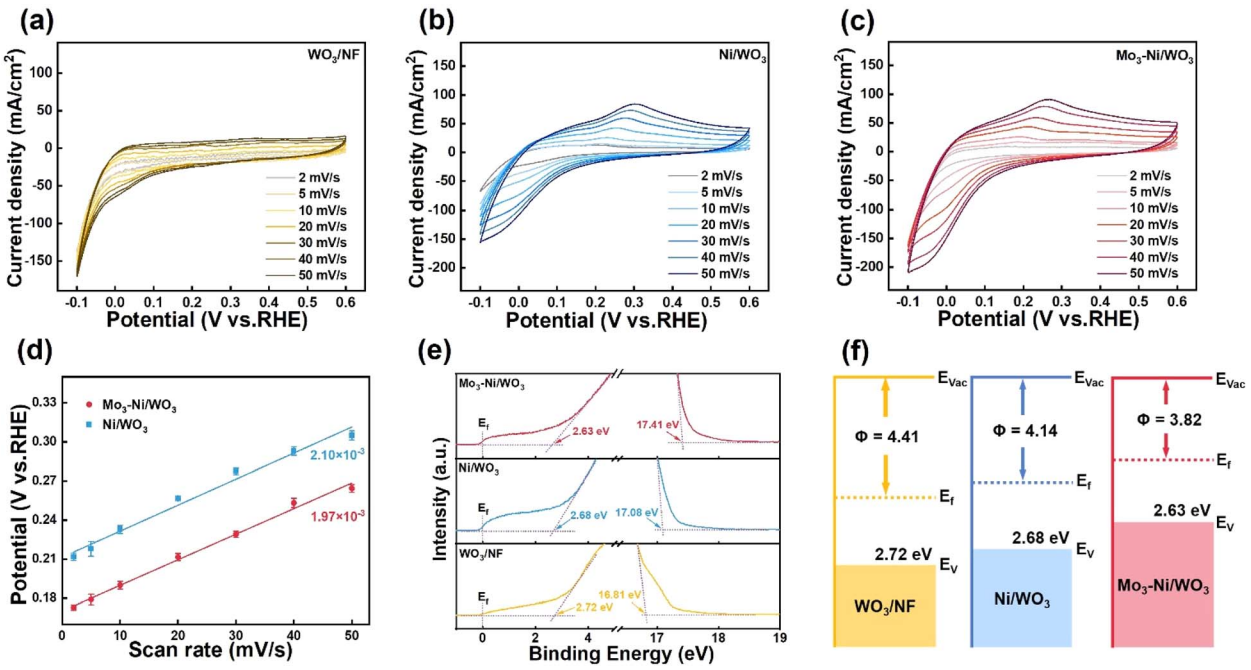

Fig. 4 WO_3/NF (a), Ni/WO_3 (b) and Mo_3–Ni/WO_3 (c) hydrogen desorption peak shifts in Ar-saturated 1 M KOH at scan rates ranging from 2 to 50 mV s^{-1}, correlation between hydrogen desorption peak positions and scan rates for Mo_3–Ni/WO_3 and Ni/WO_3 (d), UPS spectra (e), and energy band diagram of WO_3/NF, Ni/WO_3, and Mo_3–Ni/WO_3 (f).

3.3 Electrochemical measurements for the OER

The OER catalytic performance of the as-prepared catalysts was initially investigated in 1 M KOH. Fig. 5a and b shows LSV performance and current density of prepared catalysts. The optimized catalyst Mo_3–Ni/WO_3 requires only 328 mV overpotential to drive a current density of 100 mA cm^{-2}, which is lower than that of Ni/WO_3 (355 mV), WO_3/NF (561 mV), Mo_3–Ni/NF (403 mV), NF (414 mV), and RuO_2 (524 mV). The larger reconstruction peak in the Mo_3–Ni/WO_3 catalyst compared to other catalysts in a potential window of 1.35–1.45 V indicates that Ni active sites have the potential to generate large amounts of NiOOH substances through reconfiguration.[59] The Mo_3–Ni/WO_3 catalyst also manifests the lowest Tafel slope (21 mV dec^{-1}) among Ni/WO_3 (22 mV dec^{-1}), WO_3/NF (146 mV dec^{-1}), Mo_3–Ni/NF (22 mV dec^{-1}), NF (23 mV dec^{-1}), and RuO_2 (104 mV dec^{-1}), indicating faster electrode kinetics (Fig. 5c), which shows superior performance compared to other recently reported electrocatalysts in Fig. S11a. The EIS result in Fig. 5d shows the fast charge-transfer of Mo_3–Ni/WO_3. Moreover, as shown in Fig. 5e, Mo_3–Ni/WO_3 exhibits a steady current density at 100 mA cm^{-2} for 50 h. The LSV curve of Mo_3–Ni/WO_3 after 2000 cycles of CV has no obvious attenuation compared to the initial one in Fig. S11b. These results indicate that the Mo_3–Ni/WO_3 catalyst has great OER stability. Furthermore, the OER activities of other electrocatalysts with different Mo-doping levels and different electrodeposition times were also tested (Fig. S11c and d). Consistently, Mo_3–Ni/WO_3 displays the optimal electrochemical performance among other comparative catalysts.

To further identify the primary active sites of the material during the OER, *in situ* Raman spectroscopy was performed (Fig. S12). As the working voltage was gradually increased, two new Raman peaks emerged at approximately 473 cm^{-1} and 550 cm^{-1}, corresponding to the bending and stretching vibrations of the Ni–O bond, respectively.[60] These observations are indicative of the formation of the NiOOH species. As shown in Fig, S12a and b, both Mo_3–Ni/WO_3 and Ni/WO_3 underwent similar surface transformation processes; however, the optimal

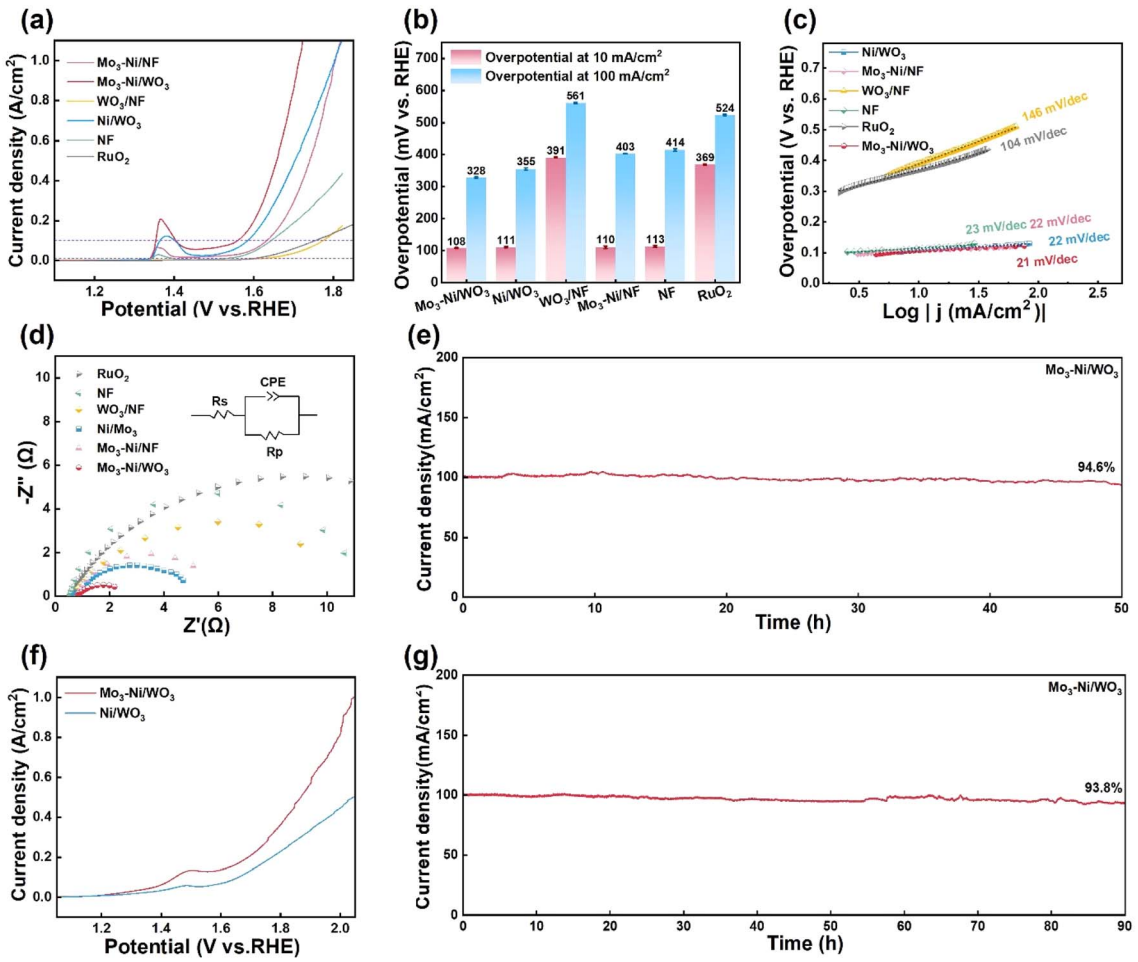

Fig. 5 Polarization LSV curves toward the OER in 1.0 M KOH (a), the overpotentials of obtained samples at different current densities (overpotential values were obtained from the average of 3 measurements) (b), Tafel slopes (c), Nyquist plot (d) of Mo_3–Ni/NF, Ni/WO_3, WO_3/NF, Mo_3–Ni/WO_3, NF, and RuO_2, and chronopotentiometry test of Mo_3–Ni/WO_3 at an initial OER current density of 100 mA cm^{-2} for 50 h (e). Polarization LSV curves of the devices based on Mo_3–Ni/WO_3 and Ni/WO_3 electrodes in 1.0 M KOH (f) and chronopotentiometry curves for Mo_3–Ni/WO_3 in a two-electrode system (g).

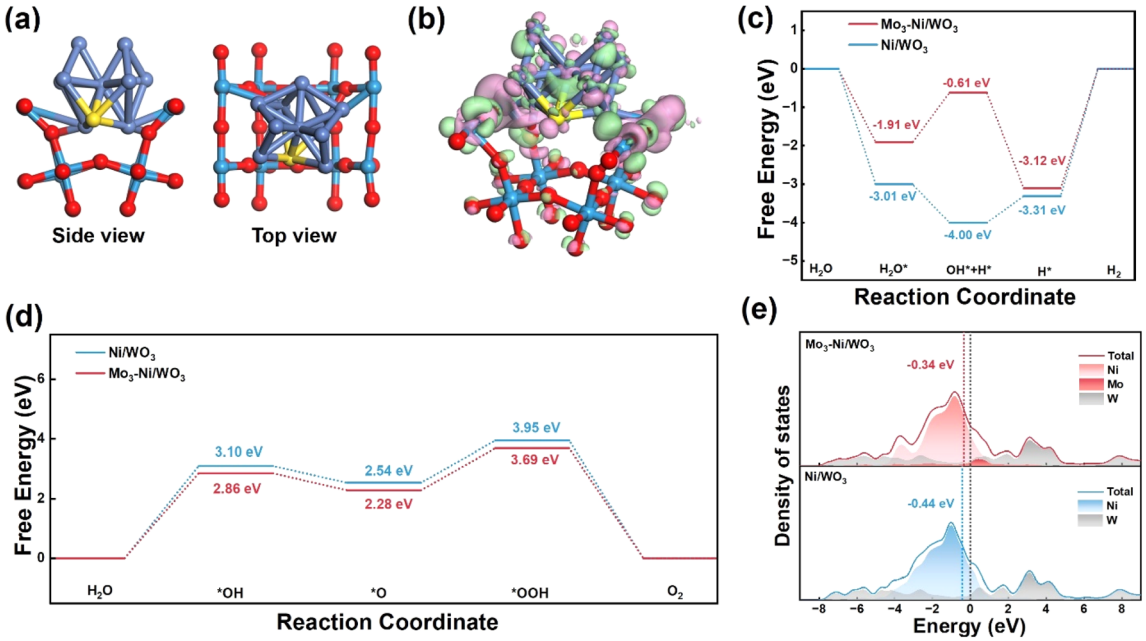

Fig. 6 Slab model of Mo_3–Ni/WO_3 (the Ni atoms are in purple, Mo in yellow, O in red, W in blue, and H in white) (a), the differential charge density of Mo_3–Ni/WO_3 (b), the Gibbs-free energy for HER kinetics on Ni sites of Mo_3–Ni/WO_3 (c), the free energy diagram of the OER processes (d), and density of states of Mo_3–Ni/WO_3 and Ni/WO_3 (e).

sample exhibited a more pronounced NiOOH peak, indicating the improved capacity to generate high-valent spices by Mo doping. Fig. S12c demonstrates that WO_3/NF displays similar Raman characteristic peaks across different applied voltages, indicating that WO_3 is not the primary active site for the OER. These findings indicate that Ni serves as the primary active site for the OER and undergoes transformation into NiOOH species *via* electrochemical reconstruction during the OER process. The constructed Ni/WO_3 heterojunction enhances the OER kinetics by establishing a BIEF and promoting interfacial charge transfer. Furthermore, Mo doping strengthens the internal electric field, thereby endowing the material with superior OER activity.[61] SEM and XRD of Mo_3–Ni/WO_3 after OER stability testing showed negligible changes as shown in Fig. S13a and b, indicating a high structural stability. In addition, the high-resolution XPS spectrum of Ni in Mo_3–Ni/WO_3 exhibits two peaks at 856.8 eV and 874.3 eV in Fig. S13d, which indicates the appearance of Ni^{3+} through surface oxidation. These results show that trivalent Ni species are generated on the Mo_3–Ni/WO_3 catalyst by reconstruction during the OER process. The high-resolution XPS spectra of W and Mo (Fig. S13e and f) almost show the same binding energies as the initial state, indicating the superior OER stability of Mo_3–Ni/WO_3.

3.4 Electrochemical measurements for water splitting

The Mo_3–Ni/WO_3 catalyst was assembled into a two-electrode cell as the cathode and anode respectively to estimate the overall water splitting performance. The Ni/WO_3 catalyst was also assembled to highlight the advantages of Mo doping for comparison. Fig. 5f shows that Mo_3–Ni/WO_3‖Mo_3–Ni/WO_3 needs only 1.69 V to drive the 200 mA cm^{-2} current density, which is better than Ni/WO_3‖Ni/WO_3. This result indicates that Mo doping in the catalyst is necessary to gain superior performance. To evaluate the faradaic efficiency, we compared the experimentally measured and theoretically calculated volumes of H_2 and O_2, as illustrated in Fig. S14. A ratio of H_2 to O_2 approaching 2 : 1 indicates that the faradaic efficiency for each gas evolution reaction is close to 100%.[61] Furthermore, stability tests of the overall water splitting cell reveal that the Mo_3–Ni/WO_3 catalyst exhibits robust performance at a current density of 100 mA cm^{-2} (Fig. 5g).

3.5 Mechanism of improving HER and OER performance of Mo_3–Ni/WO_3

The mechanism of Mo_3–Ni/WO_3 during the HER and OER was expounded through DFT calculations. The relevant information for the modelling of each catalyst is displayed in the SI, which is based on our previous work.[5,62] Fig. 6a and S15a shows the models of Mo_3–Ni/WO_3 and Ni/WO_3, which are based on the XRD and TEM results. The charge density differences in Fig. 6b indicate the distribution of electrons on Mo_3–Ni/WO_3. The pink regions represent electron accumulation, and the green regions correspond to electron depletion. This result confirms the strong charge interaction on the Ni/WO_3 heterojunction interface, which is consistent with the XPS results. The Gibbs free energy was calculated for the five stages of the HER process on Ni sites as shown in Fig. 6c. Fig. S16 and S17 shows key intermediates and transition states in Mo_3–Ni/WO_3 and Ni/WO_3, respectively, which include water adsorption, dissociation to form the H* intermediate (Volmer step), and hydrogen generation *via* either the Tafel step or the Heyrovsky step.[63] The adsorption energy of H* was reduced to −3.12 eV on the Mo_3–

Ni/WO_3 catalyst, improving the closer ideal value of 0 eV compared to that of the Ni/WO_3 catalyst. These results indicate that adsorption energy of reaction intermediates is regulated by Mo doping, enhancing the HER efficiency. Furthermore, the W site on Mo_3–Ni/WO_3 also shows ideal stats of H* adsorption compared with that of the Ni/WO_3 catalyst in Fig. S15b, which shows that W in Mo_3–Ni/WO_3 serves as an additional H* adsorption site to accelerate the HER process.

The adsorption energy of the OER process with four concerted proton–electron transfer steps was calculated according to the conventional absorbate evolution mechanism (AEM), which is shown in Fig. S18 and S19. Fig. 6d shows free energy of Mo_3–Ni/WO_3 and Ni/WO_3, indicating that the RDS of the material is OH* adsorption. The lower free energy of 2.86 eV in Mo_3–Ni/WO_3 compared to that of Ni/WO_3, 3.10 eV, indicates that the energy barrier required for the RDS in Mo_3–Ni/WO_3 during the OER is reduced by Mo doping. Besides, Mo doping induced the reduced free energy of Mo_3–Ni/WO_3 in the O* → OOH* process, which indicates that that lower energy barrier is overcome on Ni sites in Mo_3–Ni/WO_3 to generate hydroxyl oxidation species.[38,64] In addition, the total density of states (DOS) of prepared catalysts is shown in Fig. 6e. The d-band centre is closer to the Fermi level in Mo_3–Ni/WO_3, exhibiting an ideal internal electronic structure.[65,66] These results prove that Mo doping enhances the asymmetrical distribution of charge at the Ni/WO_3 heterojunction interface and constructed the BIEF, which optimizes the adsorption energy of the intermediate products and improves reaction kinetics in the HER and OER.

4 Conclusions

In conclusion, a Mo doped heterojunction catalyst (Mo_x–Ni/WO_3) was synthesized to improve the activity of the HER and OER. The dynamic adaptive function of the optimized catalyst Mo_3–Ni/WO_3 is applied to the anode and cathode in overall water splitting. The optimized catalyst Mo_3–Ni/WO_3 only needs an overpotential of 13 mV and 328 mV to achieve a current density of 10 and 100 mA cm^{-2} in the HER and OER, respectively. The exceptional catalytic activity can be attributed to the presence of element doping at the heterojunction interface. The WO_3 substrate functions as an electron acceptor, forming a BIEF in conjunction with Ni. Mo doping modulates the electron redistribution, constructs the BIEF and enhances asymmetric charge distribution on the Ni/WO_3 heterojunction, which optimizes the energy barrier of intermediates during the HER and OER process. In addition, the hydrophilic properties of the catalyst are improved, which is beneficial for the overflow of bubbles and contact between the electrode and electrolyte. This work brings out a novel avenue for the future design of heterojunction electrocatalysts for bifunctional overall water splitting.

Author contributions

Yang Sun: data curation, writing the manuscript, experimental design, formal analysis. Fan Yang: project administration, validation, funding acquisition. Kexin Wei: data curation, writing – review & editing. Siyuan Sun: validation, experimental design. Li Sun: data curation, validation. Junpu An: validation, investigation. Chunhui Yu: supervision, data curation. Qing Guo: formal analysis, supervision. Conghan Zhang: data curation, supervision. Guang Ma: validation, investigation. Hongchen Liu: methodology, validation, conceptualization. Yongfeng Li: project administration, conceptualization. All the authors have approved the final manuscript.

Conflicts of interest

There are no conflicts to declare.

Data availability

Additional data related to this paper may be obtained from the corresponding author upon request.

All data needed to support the conclusions in the paper are presented in the manuscript and the supplementary information (SI). Supplementary information: theoretical calculation method, supported electrochemical evaluation, Fig. S1–S19, and Tables S1–S3. See DOI: **https://doi.org/10.1039/d5sc06522d**.

Acknowledgements

This work was supported by the National Natural Science Foundation of China (No. 22278431).

Notes and references

1 X. Gao, Y. Chen, Y. Wang, L. Zhao, X. Zhao, J. Du, H. Wu and A. Chen, *Nano. Micro. Lett.*, 2024, **16**, 237.
2 H. Du, X. Wang, J. Song, N. Ran, J. Ma, J. Wang and J. Liu, *Adv. Funct. Mater.*, 2024, **34**, 2407586.
3 N. Esfandiari, M. Aliofkhazraei, A. N. Colli, F. C. Walsh, S. Cherevko, L. A. Kibler, M. M. Elnagar, P. D. Lund, D. Zhang, S. Omanovic and J. Lee, *P. Prog. Mater. Sci.*, 2024, **144**, 101254.
4 A. Muzammil, R. Haider, W. Wei, Y. Wan, M. Ishaq, M. Zahid, W. Yaseen and X. Yuan, *Mater. Horiz.*, 2023, **10**, 2764–2799.
5 Y. Sun, F. Yang, S. Sun, K. Wei, Y. Wang, G. Ma, J. An, J. Yuan, M. Zhao, J. Liu, H. Liu and Y. Li, *J. Colloid Interface Sci.*, 2025, **684**, 1–10.
6 W. Song, C. Xia, S. Zaman, S. Chen and C. Xiao, *Small*, 2024, **20**, 2406075.
7 L. Quan, H. Jiang, G. Mei, Y. Sun and B. You, *Chem. Rev.*, 2024, **124**, 3694–3812.
8 B. Zhou, R. Gao, J.-J. Zou and H. Yang, *Small*, 2022, **18**, 2202336.
9 G. Li, F. Yang, S. Che, H. Liu, N. Chen, J. Qian, C. Yu, J. Cheng, X. Zhang, X. Li and Y. Li, *Int. J. Hydrogen Energy*, 2024, **80**, 440–448.
10 Z.-P. Wu, X. F. Lu, S.-Q. Zang and X. W. Lou, *Adv. Funct. Mater.*, 2020, **30**, 1910274.

11 J. Liu, W. Qiao, Z. Zhu, J. Hu and X. Xu, *Small*, 2022, **18**, 2202434.
12 Q. Zhang, B. Liu, L. Li, Y. Ji, C. Wang, L. Zhang and Z. Su, *Small*, 2021, **17**, 2005769.
13 X. Zhou, T. Yang, T. Li, Y. Zi, S. Zhang, L. Yang, Y. Liu, J. Yang and J. Tang, *Nano Res. Energy*, 2023, **2**, e9120086.
14 L. Dai, Z.-N. Chen, L. Li, P. Yin, Z. Liu and H. Zhang, *Adv. Mater.*, 2020, **32**, 1906915.
15 Y. Luo, Z. Zhang, F. Yang, J. Li, Z. Liu, W. Ren, S. Zhang and B. Liu, *Energy Environ. Sci.*, 2021, **14**, 4610–4619.
16 Z. Ma, S. Zhan, Y. Xie, Y. Liu, Y. Ding, S. Zhang, H. Lin, L. Zhang, T. Liu and Y. Xie, *Adv. Mater.*, 2025, 2420565.
17 P. Wang, R. Qin, P. Ji, Z. Pu, J. Zhu, C. Lin, Y. Zhao, H. Tang, W. Li and S. Mu, *Small*, 2020, **16**, 2001642.
18 Y. Sun, S. Zhou, N. Yang, H. Shen, X. Yang, L. Zhang, X. Xiao, B. Jiang and L. Zhang, *J. Colloid Interface Sci.*, 2025, **688**, 1–10.
19 D. Zhou, J. Yu, J. Tang, X.-Y. Li and P. Ou, *Adv. Funct. Mater.*, 2025, **15**, 2404007.
20 X. Fan, B. Li, C. Zhu, F. Yan, X. Zhang and Y. Chen, *Small*, 2024, **20**, 2309655.
21 X. Zhang, Y. Dong, Q. Lv, F. wang, C. Jiang, Y. Wang, J. Dou, Q. Guo, B. Dong and Q. Tang, *Appl. Catal., B*, 2024, **342**, 123440.
22 B. Zhou, J. Wang, L. Guo, H. Li, W. Xiao, G. Xu, D. Chen, C. Li, Y. Du, H. Ding, Y. Zhang, Z. Wu and L. Wang, *Adv. Energy Mater.*, 2024, **14**, 2402372.
23 T. Zhang, J. Liu, K. Zhu, Y. Hu, R. Liu, J. Chen, C. Jiang and J. Chen, *Mater. Sci. Eng. B*, 2023, **298**, 116847.
24 L. Li, X. Zhao, D. Pan and G. Li, *Chin. J. Catal.*, 2017, **38**, 2132–2140.
25 S. Yu, J. Li, J. Yin, W. Liang, Y. Zhang, T. Liu, M. Hu, Y. Wang, Z. Wu, Y. Zhang and Y. Du, *Chin. Chem. Lett.*, 2024, **35**, 110068.
26 H. Liu, F. Yang, F. Chen, S. Che, N. Chen, S. Sun, N. Ta, Y. Sun, N. Wu, Y. Sun and Y. Li, *J. Colloid Interface Sci.*, 2023, **640**, 1040–1051.
27 G. Li, F. Yang, S. Che, H. Liu, N. Chen, J. Qian, C. Yu, B. Jiang, M. Liu and Y. Li, *J. Mater. Sci. Technol.*, 2023, **166**, 58–66.
28 S. Ge, X. Shen, J. Gao, K. Ma, H. Zhao, R. Fu, C. Feng, Y. Zhao, Q. Jiao and H. Li, *Chem.–Eng. J.*, 2024, **485**, 150161.
29 J. Ni, Y. Zhao, L. Li and L. Mai, *Nano. Energy.*, 2015, **11**, 129–135.
30 J. Diao, W. Yuan, Y. Qiu, L. Cheng and X. Guo, *J. Mater. Chem. A*, 2019, **7**, 6730–6739.
31 W. Peng, W. Zhang, Y. Lu, W. Li, J. He, D. Zhou, W. Hu and X. Zhong, *J. Colloid Interface Sci.*, 2024, **664**, 980–991.
32 Y. Sun, F. Yang, S. Sun, Y. Sun, H. Liu, C. Yu, J. An, X. Li and Y. Li, *Fuel*, 2024, **366**, 131399.
33 Z. Wang and S. Wang, *Appl. Catal., B*, 2024, **352**, 124002.
34 S. Hou, Y. Xu, Z. Chen, G. Yang, C. Zhu, X. Fan, X. Weng, J. Wang, L. Wang and Y. Cui, *ACS Catal.*, 2024, **14**, 8238–8251.
35 X. Zhou, J. Li, G. Zhou, W. Huang, Y. Zhang, J. Yang, H. Pang, M. Zhang, D. Sun, Y. Tang and L. Xu, *J. Energy Chem.*, 2024, **93**, 592–600.
36 L. Sun, M. Feng, Y. Peng, X. Zhao, Y. Shao, X. Yue and S. Huang, *J. Mater. Chem. A*, 2024, **12**, 8796–8804.
37 M. Fang, Q. Cai, Q. Qin, W. Hong and W. Liu, *Chem.–Eng. J.*, 2021, **421**, 127796.
38 L. Yan, G. Dong, X. Huang, Y. Zhang and Y. Bi, *Appl. Catal., B*, 2024, **345**, 123682.
39 J. Kim, S.-M. Jung, N. Lee, K.-S. Kim, Y.-T. Kim and J. K. Kim, *Adv. Mater.*, 2023, **35**, 2305844.
40 H. Wang, Y. Jiao, G. Zhang, Z. Zhang, W. Ma, C. Sun and X. Zong, *Chem.–Eng. J.*, 2024, **497**, 154776.
41 L. Xiao, C. Cheng, T. Yang, J. Zhang, Y. Han, C. Han, W. Lv, H. Tan, X. Zhao, P. Yin, C. Dong, H. Liu, X. Du and J. Yang, *Adv. Mater.*, 2024, **36**, 2411134.
42 X. Zhu, C. Tang, H.-F. Wang, B.-Q. Li, Q. Zhang, C. Li, C. Yang and F. Wei, *J. Mater. Chem. A*, 2016, **4**, 7245–7250.
43 S. Jeong, U. Kim, S. Lee, Y. Zhang, E. Son, K.-J. Choi, Y.-K. Han, J. M. Baik and H. Park, *ACS Nano*, 2024, **18**, 7558–7569.
44 Z. Du, X. Cheng, X. Yang, G. Ran, H. Liu, S. He and Z. Hua, *J. Colloid Interface Sci.*, 2025, **677**, 665–676.
45 T. Li, J. Yin, D. Sun, M. Zhang, H. Pang, L. Xu, Y. Zhang, J. Yang, Y. Tang and J. Xue, *Small*, 2022, **18**, 2106592.
46 J. Song, Y. Q. Jin, L. Zhang, P. Dong, J. Li, F. Xie, H. Zhang, J. Chen, Y. Jin, H. Meng and X. Sun, *Adv. Energy Mater.*, 2021, **11**, 2003511.
47 W. Liang, M. Zhou, X. Lin, J. Xu, P. Dong, Z. Le, M. Yang, J. Chen, F. Xie, N. Wang, Y. Jin and H. Meng, *Appl. Catal., B*, 2023, **325**, 122397.
48 C. Feng, M. Chen, Y. Zhou, Z. Xie, X. Li, P. Xiaokaiti, Y. Kansha, A. Abudula and G. Guan, *J. Colloid Interface Sci.*, 2023, **645**, 724–734.
49 R. Shi, Y. Li, X. Xu, X. Wang and G. Zhou, *Adv. Funct. Mater.*, 2024, **34**, 2409849.
50 Y. Fan, Y. Gu, D. Wang, Y. Jiao, A. Wu and C. Tian, *J. Energy Chem.*, 2024, **95**, 428–439.
51 X. Jiang, V. Kyriakou, C. Song, X. Wang, S. Costil, C. Deng, T. Liu, T. Jiang and H. Liao, *J. Energy Chem.*, 2024, **93**, 511–518.
52 X. Luo, P. Ji, P. Wang, R. Cheng, D. Chen, C. Lin, J. Zhang, J. He, Z. Shi, N. Li, S. Xiao and S. Mu, *Adv. Energy Mater.*, 2020, **10**, 1903891.
53 X. Wang, M. Yu, C. Lv, L. Wang, W. Kan, G. Xu, L. Sun and B. Zhao, *FlatChem*, 2024, **45**, 100660.
54 T. Ren, Q. Chen, C. Tang, J. Chen, X. Huang, G. Feng, H. Xie, F. Bao and W. Guo, *Fuel*, 2025, **381**, 133302.
55 J. Chang, F. Song, Y. Hou, D. Wu, F. Xu, K. Jiang and Z. Gao, *J. Colloid Interface Sci.*, 2024, **665**, 152–162.
56 Y. Yang, W. Zheng, P. Wang, Z. Cheng, P. Wang, J. Yang, C. Wang, J. Chen, Y. Qu, D. Wang and Q. Chen, *ACS Nano*, 2024, **18**, 24458–24468.
57 J. Li, Y. Tan, M. Zhang, W. Gou, S. Zhang, Y. Ma, J. Hu and Y. Qu, *ACS Energy Lett.*, 2022, **7**, 1330–1337.
58 X. Yang, H. Shen, X. Xiao, Z. Li, Q. Zhou, W. Yang, B. Jiang, Y. Sun, L. Zhang and Z. Yan, *J. Energy Chem.*, 2025, **100**, 26–38.

59 W. Zhang, L. Yang, Z. Li, G. Nie, X. Cao, Z. Fang, X. Wang, S. Ramakrishna, Y. Long and L. Jiao, *Angew. Chem., Int. Ed.*, 2024, **63**, e202400888.
60 Y. Li, Z. Zhang, C. Li, Y. Zhou, X.-B. Chen, H. Lu, Z. Shi and S. Feng, *Appl. Catal., B*, 2024, **355**, 124116.
61 D. Rathore, A. Banerjee and S. Pande, *ACS Appl. Nano Mater.*, 2022, **5**, 2664–2677.
62 X. Luo, P. Ji, P. Wang, R. Cheng, D. Chen, C. Lin, J. Zhang, J. He, Z. Shi, N. Li, S. Xiao and S. Mu, *Adv. Energy Mater.*, 2020, **10**, 1903891.
63 G. Li, M. Zhao, F. Yang, H. Liu, J. Wang, J. Ren and Y. Li, *Int. J. Hydrogen Energy*, 2025, **105**, 1–9.
64 H. Liu, X. Yan, F. Yang, S. Che, J. Wang, J. Qian, X. Zhang, S. Sun, Y. Sun, N. Wu, S. Wang and Y. Li, *Int. J. Hydrogen Energy*, 2024, **56**, 725–734.
65 X. Yu, T. Fang, X. Han, J. Gao and Y. Ma, *Appl. Catal., B*, 2025, **361**, 124636.
66 M. Chen, Z. Du, N. Liu, H. Li, J. Qi, E. Shangguan, J. Li, J. Cao, S. Yang, W. Zhang and R. Cao, *Chin. J. Catal.*, 2025, **69**, 282–291.